Available online at www.sciencedirect.com
ScienceDirect
International Journal of Heat and Mass Transfer 50 (2007) 240–256
International Journal of HEAT and MASS TRANSFER
www.elsevier.com/locate/ijhmt

Transient heat, mass and momentum transfer of an evaporating stationary droplet containing dissolved cerium nitrate in a rf thermal argon–oxygen plasma under reduced pressure

I. Castillo, R.J. Munz *

Department of Chemical Engineering, McGill University, 3610 University St., Montreal, Que., Canada H3A 2B2

Received 23 January 2006
Available online 8 September 2006

Abstract

Heat and mass transfer effects in evaporating solution droplets (20–40 μm in diameter) containing dissolved hexahydrated cerium nitrate in a stationary rf $Ar–O_2$ thermal plasma were investigated using a model. The evaporation occurred under reduced pressure. The impact of different plasma operating parameters on temperature and dissolved solid content profiles was studied: surrounding plasma temperature, initial salt content and droplet size, plasma gas composition, and system pressure. Temperature and composition dependant thermophysical properties were used. The model was solved in a moving frame (ALE method) and considered Stefan flow. The results indicate that a salt supersaturation limit is reached at the droplet surface which leads to salt precipitation and formation of a crust in all cases analyzed. This is favored by higher plasma temperatures, lower pressures, oxygen-rich plasma and higher salt content. Smaller droplets developed a crust faster than larger droplets.

Keywords: Evaporation; Solution droplets; ALE; Thermal plasma; Solid oxide fuel cells

1. Introduction

The manufacturing of ceramic powders from liquid precursors using radio frequency (rf) thermal plasmas has been developed in the past 10 years [1–5]. This technique consists of the evaporation and calcination of atomized solution or suspension droplets injected axially to the plasma core. In this paper only the case of solution droplets was investigated. Most of these processes are operated under reduced pressure and the droplets usually contain a non-volatile salt (nitrates, acetates, chlorides, etc.) dissolved in water or any other suitable solvent. The hot plasma environment provides the driving force for evaporation and calcination of the salt, resulting in the production of high-purity oxide particles. Thus, oxygen-rich plasmas are often employed. The use of liquid precursors encompasses applications such as production of ceramic materials for SOFC (solid oxide fuel cells) (perovskites, Y_2O_3, CeO_2, NiO, etc.) [6] and thermal barrier coatings (ZrO_2) [7].

One of the main advantages of rf thermal plasma over other processing techniques is the ability to achieve a uniform chemical composition in the synthesized particles in a clean electrode-free environment. It has been shown that the stoichiometry of these powders can be controlled accurately even when doped oxide particles are synthesized [8]. However, the resulting particles varied greatly in size from few nanometers to micron size, suggesting that more than one droplet-to-particle conversion mechanism was possible. Few attempts have been conducted to understand this large size variation by sampling particles in-flight [9], largely due to the high plasma temperatures and the inaccessibility of sampling in the plasma core. Therefore, studying the droplet-to-particle conversion in rf thermal plasmas through numerical simulation seems to be a logical alternative.

* Corresponding author. Tel.: +1 514 398 4277; fax: +1 514 398 6678.
E-mail address: richard.munz@mcgill.ca (R.J. Munz).

0017-9310/$ - see front matter © 2006 Elsevier Ltd. All rights reserved.
doi:10.1016/j.ijheatmasstransfer.2006.06.023

Nomenclature

C	convective velocity (relative velocity between the material V and mesh velocity Ψ) [m/s]
C_i	concentration of electrolyte i [mol/L]
C_s	concentration of salt at the droplet surface
C_m	mean concentration of salt in the droplet
C_p	heat capacity [J/kg K]
D_{12}	diffusion coefficient based on molecular concentration [m^2/s]
d	droplet diameter [μm]
F	Faraday constant
h	enthalpy [J/kg]
K	evaporation constant [m^2/s]
K_p	partition coefficient
k	thermal conductivity [W/m K]
m	molality of the solute [mol/kg solvent]
$\dot{m}$	mass flow rate at the droplet surface due to vaporization, [kg/m^2s]
M	molecular weight [kg/kg mol]
M_{av}	average gas molecular weight [kg/kg mol]
P	pressure [Pa]
Q	source/sink term [J/m^3s]
r	radial distance [m]
$R_{(t)}$	radius of the droplet (function of time) [m]
R_g	universal gas constant
$\dot{R}$	change of droplet radius with respect to time [m/s]
T	temperature [K]
T_d	dimensionless temperature
t	time [s]
T_r	reference temperature [K]
V	radial material velocity [m/s]
W_i	mass fraction of i in liquid
x_i	mol fraction of i in liquid
Y_i	mass fraction of i in gas
z_i	mol fraction of i in gas

Greek symbols

$\gamma_{\pm}$	mean ionic activity coefficient of the solute
λ^0_+, λ^0_-	limiting (zero concentration) ionic conductances [$(A/cm^2)(V/cm)(mol/cm^3)$]
μ	plasma gas viscosity [kg/m s]
μ_1	water viscosity in the droplet [kg/m s]
ρ	density [kg/m^3]
σ_i	coefficient characteristic of each ion
υ_+, υ_-	valences of cation and anion, respectively
Ψ	mesh velocity [m/s]

Subscripts

1	component 1 (either in the solution or the gas phase)
2	component 2 (either in the solution or the gas phase)
ar	argon
d	dimensionless
G	plasma gas phase
L	solution droplet phase
0	initial value
ox	oxygen
s	anhydrous salt
w	water
χ	referential domain or moving mesh
∞	conditions at infinity (far away from the droplet)

Superscript

S	saturated condition

Droplets are injected into the plasma core by means of a liquid blast atomizer that provides a log-normal droplet size distribution centered around 20–30 μm in diameter. This process is similar to the well known spray pyrolysis technique [10], but the operating temperatures are higher, the droplets are often in the low micro size range (<50 μm) and the reactor chamber is operated under vacuum. As a result, the thermal plasma treatment is a more "rapid" version of spray pyrolysis, since the conditions for solvent evaporation are enhanced. Previous theoretical and experimental studies in spray pyrolysis of non-volatile solute droplets have suggested the development of a thin crust surrounding the evaporating droplet. The crust is formed because the non-volatile salt precipitates out of solution, primarily at the droplet surface. A fast evaporation rate removes solvent from the droplet surface more quickly than it can be replenished by mass diffusion, resulting in the formation of a crust [11]. Having a crust around an evaporating liquid core retards the rate at which inner solvent escapes from the droplet [12], because the solvent must travel through a solid phase. This effect leads to an increase of the solvent vapor pressure that causes fracturing and/or bursting of the crust. As a consequence, after calcination takes place, solid particles of different sizes are formed. A recent study by Ozturk and Cetegen [13] has shown that solid and hollow particles of ZrO_2 can be produced using thermal plasmas from zirconium acetate depending on the plasma operating conditions. Ozturk's findings provide evidence that a comprehensive model explaining droplet-to-particle conversion is needed.

Evaporating droplets were first studied experimentally and theoretically by Charlesworth and Marshall [11]. They suspended droplets containing various dissolved salts in a hot-air stream and pointed out that mass diffusion in the droplet played a key role in determining the onset of salt precipitation. The work of Schlünder [14] and Gardner [15] demonstrated that the product of the drop radius times its rate of change over time remained constant for most of

the evaporation process. More recently, Xiong and Kodas [16] investigated the spray pyrolysis of sodium chloride solution drops in air. In this comprehensive study small micron size droplets [1–10 μm] were examined. It was reported that the point of solute nucleation was relatively independent of processing parameters, except solution concentration and initial droplet size. Their findings were based on the evaporation of droplets in air at atmospheric pressure. The change in droplet diameter was not rigorously calculated from the solution of the heat and mass transfer between the drop and the surrounding media. A more formal treatment of the solution of the mass and heat transport equations of these phenomena was conducted by Javanthi et al. [17]. It was found that droplet shrinkage and solute diffusion were the rate limiting processes, because their characteristic time constants were larger than those of heat conduction inside and outside the droplet and vapor diffusion outside the droplet. However, bulk flow as a result of solvent evaporation was neglected in this study. A rigorous approach of droplet evaporation was reported by Elperin and Krasovitov [12] for the case of slurry droplets, but it was assumed that the evaporation stage resembled that of a pure component droplet. Therefore, there is a need for a rigorous treatment of evaporating solutions droplets when heat-mass-momentum transfers are considered. Also the rate of shrinkage of droplets over time must be taken into account.

In this paper, the effect of temperature, pressure, gas composition, initial solid content and initial droplet size were examined on evaporating solution droplets under thermal plasma conditions. The droplets contained a hexahydrated salt, $Ce(NO_3)_3 \cdot 6H_2O$, dissolved in water and the mass and thermal history inside the droplet were studied. The hexahydrated cerium nitrate salt was used as a precursor to obtain CeO_2, which is used as electrolyte material in SOFCs. The onset of salt precipitation was predicted as a function of different parameters. The droplet was allowed to decrease in size as water was continuously being evaporating. The purpose of this study is to derive understanding of how plasma conditions affect droplet morphology and to predict the onset of crust formation under typical rf thermal plasma operating conditions.

2. Model development

The physical model studied was the transient evaporation of a solution droplet of approximately 30 μm in diameter immersed in a mixture of stagnant argon–oxygen rf plasma. The solution droplet was a hexahydrated salt, $Ce(NO_3)_3 \cdot 6H_2O$, dissolved in water. The dissolved salt released all water of hydration and thus the total water content in the droplet was a combination of water of hydration and water already present in the solution. The anhydrous salt was considered to remain largely in molecular form (i.e. as $Ce(NO_3)_3$), since the solution droplet possessed a large salt content, but whenever possible the properties were calculated assuming dissociation of the nitrate and the cerium ions.

Radiation and second-order effects, such as Soret and Dufor effects, were assumed to be negligible, but Stefan flow was taken into account. This flow is representative of the diffusional transport of energy. The droplet was considered to be suddenly immersed in a stagnant plasma gas and it reduced in size as water evaporated but remained spherical. Plasma gas absorption on the surface was neglected based on the low system pressures. Spherical symmetry reduced the problem to a transient, two phase process of one dimensional nature. The only fluid motion present was a radial flow field in the gas phase induced by water vaporization. Radial flow inside the droplet was neglected on the basis of the large density difference between the solution droplet and the gas. Viscous dissipation effects were neglected. Water evaporation occurred at the droplet–gas interphase and both gas and liquid phases are treated as ideal phases. The Kelvin effect due to droplet curvature on the equilibrium vapor pressure was negligible since the size of the droplet is larger than 1 μm. Finally, the surrounding gas obeyed the ideal gas law. All the model results were calculated using variable thermophysical properties, except when the comparison between variable and constant properties was made.

Under these conditions the physics of the problem were as follows (Fig. 1): solvent (i.e. water) evaporates from the solution droplet which causes droplet shrinkage, the remaining salt diffuses toward the centre of the droplet

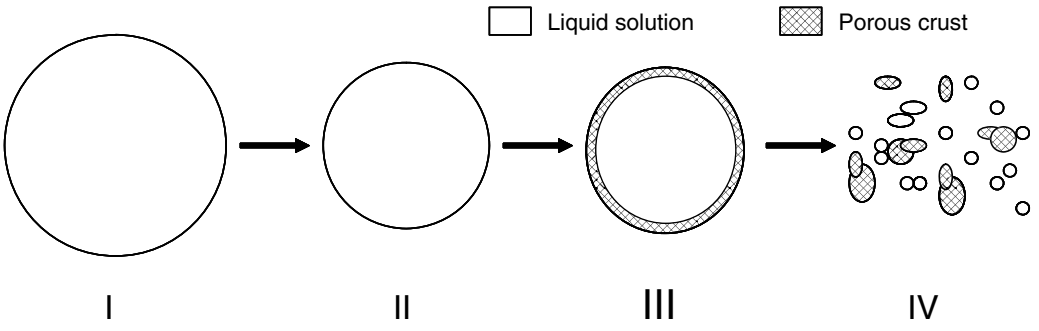

Fig. 1. Schematic of evaporating droplet history.

and a temperature profile is developed in the droplet. The solvent vapors mix with the surrounding gas as a result of bulk flow and diffusion. A temperature profile also develops in the gas phase. This process occurs until the surface of the droplet reaches the supersaturation limit of the solution and salt precipitates out as small solid "clusters". At this point the most widely accepted theory is that continuing solvent evaporation increases the number of precipitated clusters and favors cluster agglomeration as the droplet reduces in size. This results in the formation of a porous and thin crust at the droplet surface (Fig. 1, II and III). The droplet [10], surface tension forces keep the solution droplet spherical. It is then hypothesized that the precipitate undergoes thermolysis and the $Ce(NO_3)_3$ salt is transformed into CeO_2, followed by sintering. The present study only considered the problem until the saturation point (Fig. 1, III) was reached at the surface of the droplet and the later phenomena are the subject of future investigation.

This model was solved using the Arbitrary-Lagrangian–Eulerian (ALE) method which has been successfully employed with moving boundary problems [18]. A deformed mesh can be useful when the boundaries of the computational domain are moving in time as a function of a parameter, in this case, the rate of evaporation of the solution droplet. Therefore, a new mesh is not needed to be generated for each configuration of the boundaries; instead the mesh nodes are perturbed so that they conform to the moved boundaries [19]. In doing so, computational time could be saved without losing resolution in the solution.

2.1. Liquid governing equations

For the liquid phase, $r < R(t)$, (1) refers to the water and (2) refers to the anhydrous salt (i.e. $Ce(NO_3)_3$). Note that the term containing h_1 and h_2 in the energy equation for both the liquid and gas phases is representative of the Stefan flow:

Species equation

$$\frac{\partial}{\partial t}(r^2\rho_{\mathrm{L}}W_1)\bigg|_{\chi}+\frac{\partial}{\partial r}\left(-r^2\rho_{\mathrm{L}}D_{\mathrm{L}}\frac{\partial W_1}{\partial r}\right)=0 \tag{1}$$

Energy equation

$$\frac{\partial}{\partial t}(r^2\rho_{\mathrm{L}}C_{p_{\mathrm{L}}}T)\bigg|_{\chi}+\frac{\partial}{\partial r}\left(-r^2k_{\mathrm{L}}\frac{\partial T}{\partial r}-r^2\rho_{\mathrm{L}}D_{\mathrm{L}}\frac{\partial W_1}{\partial r}(h_1-h_2)\right)=0 \tag{2}$$

2.2. Gas governing equations

For the gas phase, $r > R(t)$, (1) refers to the water and (2) refers to the plasma gas argon–oxygen mixture. The convective velocity is defined as $C = V - \psi$:

Continuity equation

$$r^2\frac{\partial\rho_{\mathrm{G}}}{\partial t}\bigg|_{\chi}+\rho_{\mathrm{G}}\left(r^2\frac{\partial V}{\partial r}+2rV\right)+r^2C\frac{\partial\rho_{\mathrm{G}}}{\partial r}=0 \tag{3}$$

Species equation

$$\frac{\partial}{\partial t}(r^2\rho_{\mathrm{G}}Y_1)\bigg|_{\chi}+\frac{\partial}{\partial r}\left(-r^2\rho_{\mathrm{G}}D_{\mathrm{G}}\frac{\partial Y_1}{\partial r}+r^2\rho_{\mathrm{G}}Y_1C\right)=0 \tag{4}$$

Energy equation

$$\frac{\partial}{\partial t}(r^2\rho_{\mathrm{G}}C_{p_{\mathrm{G}}}T)\bigg|_{\chi}+\frac{\partial}{\partial r}\left(-r^2k_{\mathrm{G}}\frac{\partial T}{\partial r}-r^2\rho_{\mathrm{G}}D_{\mathrm{G}}\frac{\partial Y_1}{\partial r}(h_1-h_2)+r^2\rho_{\mathrm{G}}C_{p_{\mathrm{G}}}TC\right)=Q,$$

$$Q=-P\left(\frac{\partial V}{\partial r}\right) \tag{5}$$

Momentum equation

$$\frac{\partial}{\partial t}(r^2\rho_{\mathrm{G}}V)\bigg|_{\chi}=\frac{\partial}{\partial r}\left(r^2\left[2\mu\frac{\partial V}{\partial r}-P\right]\right)+r^2\left(F-\rho C\frac{\partial V}{\partial r}-\frac{2(2\mu V/r-P)}{r}\right),$$

$$F=-\frac{\partial}{\partial r}\left(\frac{2}{3}\mu\left(\frac{\partial V}{\partial r}\right)\right) \tag{6}$$

2.3. Boundary conditions

At liquid/gas interface:

Overall mass

$$\dot{m}=\rho_{\mathrm{G}}(V-\dot{R})_{\mathrm{G}}=\rho_{\mathrm{L}}(0-\dot{R})_{\mathrm{L}} \tag{7}$$

Species balance

$$(n_{i\mathrm{G}}-\dot{R}\rho_{\mathrm{G}})_{\mathrm{G}}=(n_{i\mathrm{L}}-\dot{R}\rho_{\mathrm{L}})_{\mathrm{L}};$$

$$n_{i\mathrm{G}}=\rho_{\mathrm{G}}Y_iV-\rho_{\mathrm{G}}D_{\mathrm{G}}\frac{\partial Y_i}{\partial r};\quad n_{i\mathrm{L}}=-\rho_{\mathrm{L}}D_{\mathrm{L}}\frac{\partial W_i}{\partial r} \tag{8}$$

Energy balance

$$\left(e_{\mathrm{G}}-\dot{R}\sum_{i=1}^{n}\rho_{\mathrm{G}}Y_ih_{i\mathrm{G}}\right)_{\mathrm{G}}=\left(e_{\mathrm{L}}-\dot{R}\sum_{i=1}^{n}\rho_{\mathrm{L}}W_ih_{i\mathrm{L}}\right)_{\mathrm{L}};$$

$$e_{\mathrm{G}}=-k_{\mathrm{G}}\frac{\partial T}{\partial r}+\sum_{i=1}^{n}n_{i\mathrm{G}}h_{i\mathrm{G}};\quad e_{\mathrm{L}}=-k_{\mathrm{L}}\frac{\partial T}{\partial r}+\sum_{i=1}^{n}n_{i\mathrm{L}}h_{i\mathrm{L}} \tag{9}$$

Thermodynamics

$$Pz_i=P_i^s\gamma_ix_i,\quad \gamma_i=1\quad\text{and}\quad K_{\mathrm{p}}=\frac{P_i^s}{P} \tag{10}$$

The mol fractions z_i and x_i can be expressed in their corresponding mass fractions Y_i and W_i (considering their respective molecular masses M_{G}, M_{w}, M_{s}). Solving for the mass fraction of water in the gas (Y_i) Eq. (10) gives Eq. (11).

$$Y_1=\left\{\frac{M_{\mathrm{G}}}{M_{\mathrm{w}}K_{\mathrm{p}}}\left(1+\frac{M_{\mathrm{w}}}{M_{\mathrm{s}}}\left(\frac{1}{W_1}-1\right)-K_{\mathrm{p}}\right)+1\right\}^{-1} \tag{11}$$

Temperature

$$T_{\mathrm{G}}=T_{\mathrm{L}} \tag{12}$$

Table 1
Thermophysical properties

Property	Method	Mixing rule
Liquid properties		
Density [kg/m^3]	Ideal mixing	$\rho_L = aW_1 + bW_2$; $a = 1000$; $b = 1600$[a]
Specific heat [J/kg K]	Ideal mixing	$C_{p_1} = a + bT + cT^2 + dT^3$, $a = 8.958 \times 10^3$, $b = -4.053 \times 10^1$, $c = 1.124 \times 10^{-1}$, $d = -1.014 \times 10^{-4}$ [22] $C_{p_2} = 358.06$ [23] $C_{p_L} = C_{p_1}W_1 + C_{p_2}W_2$
Thermal conductivity [W/m K]	Riedel for aqueous solutions [24]	$k_{1(T_r)} = a + bT + cT^2$; $a = -3.838 \times 10^{-1}$, $b = 5.254 \times 10^{-3}$, $c = -6.369 \times 10^{-6}$ $k_{L(T_r)} = k_{1(T_r)} + \Sigma\sigma_i C_i$; $\sigma(NO_3^-) = -6.978 \times 10^{-5}$; $\sigma(Ce^{4+}) = -43.61 \times 10^{-5}$ $k_{L(T)} = k_{L(T_r)} * k_{1(T)}/k_{1(T_r)}$
Binary diffusion coefficient [m^2/s]	Nerst–Haskell equation and Gordon approach for concentrated solutions [24]	$D^0_{12} = R_g T/F^2 * (1/\upsilon_+ + 1/\upsilon_-)/(1/\lambda^0_+ + 1/\lambda^0_-)/1 \times 10^4$; $D_{12(T_r)} = D^0_{12}(\eta_s/\eta)(\rho_s V_s) * (1 + m\partial \ln \gamma_\pm/\partial m)$[c] $D_{12(T)} = D_{12(T_r)}(T/T_r)(\mu_{1(T_r)}/\mu_{1(T)})$ $\partial \ln \gamma_\pm/\partial m$ [25][b]
Water viscosity [kg/m s]		$M_1 = a + bT + cT^2 + dT^3$; $a = -2.471 \times 10^1$, $b = 4.209 \times 10^3$, $c = 4.527 \times 10^{-2}$, $d = -3.376 \times 10^{-5}$ [24]
Enthalpy of water [J/kg]		$h_1 = a + bT + cT^2 + dT^3$; $a = -2.248 \times 10^6$, $b = 1.297 \times 10^4$, $c = -2.291 \times 10^1$, $d = 1.962 \times 10^{-2}$
Enthalpy of $Ce(NO_3)_3$ salt [J/kg]		$H_2 = h^0_2 + C_{p_2}(T - T_r)$
Gas properties		
Density [kg/m^3]	Ideal gas	$P = PM_{av}/R_g T$
Specific heat [J/kg K]	Ideal mixing	$C_{p_1} = a + bT + cT^2 + dT^3 + eT^4$, $a = 1.652 \times 10^3$, $b = 1.295 \times 10^{-1}$, $c = 1.850 \times 10^{-3}$, $d = -1.959 \times 10^{-6}$, $e = 6.384 \times 10^{-10}$ [26] $C_{p_{ox}} = a + bT + cT^2 + dT^3$, $a = 8.958 \times 10^3$, $b = -4.053 \times 10^1$, $c = 1.124 \times 10^{-1}$, $d = -1.014 \times 10^{-4}$ $C_{p_{ar}} = 520.4$ [27] $C_{p_2} = Y_{ar}M_{ar} + Y_{ox}M_{ox}$ $C_{p_G} = C_{p_1}Y_1 + C_{p_2}M_2$
Thermal conductivity [W/m K]	Wassiljewa equation with the Mason and Saxena modification [24]	$K_1 = a + bT + cT^2 + dT^3 + eT^4 + fT^5$; $a = -1.134 \times 10^{-2}$, $b = 2.402 \times 10^{-4}$, $c = -6.519 \times 10^{-7}$, $d = 9.231 \times 10^{-10}$, $e = -5.506 \times 10^{-13}$, $f = 9.944 \times 10^{-17}$, $k_{ar} = a + bT$; $a = 1.944 \times 10^{-2}$, $b = 2.464 \times 10^{-5}$, $k_{ox} = a + bT + cT^2 + dT^3$; $a = -1.197 \times 10^{-2}$, $b = 1.342 \times 10^{-4}$, $c = -6.456 \times 10^{-8}$, $d = 1.782 \times 10^{-11}$, $k_G = z_1k_1/(z_1 + z_2\Phi_{12}) + z_2k_2/(z_2 + z_1\Phi_{21})$[e]
Viscosity [kg/m s]	Wassiljewa equation with the Mason and Saxena modification [24]	$M_1 = a + bT + cT^2 + dT^3$; $a = -5.424 \times 10^{-6}$, $b = 4.855 \times 10^{-8}$, $c = -5.722 \times 10^{-12}$, $d = -2.946 \times 10^{-16}$ $\mu_{ar} = a + bT$; $a = 2.975 \times 10^{-5}$, $b = 2.893 \times 10^{-8}$ $\mu_{ox} = a + bT$; $a = 2.326 \times 10^{-5}$, $b = 2.799 \times 10^{-8}$ $\mu_G = z_1\mu_1/(z_1 + z_2\Phi_{12}) + z_2\mu_2/(z_2 + z_1\Phi_{21})$, $\Phi_{12} = [1 + (\mu_1/\mu_1)^{1/2}(M_2/M_1)^{1/4}]^2/[8(1 + (M_1/M_2))]^{1/2}$, $\Phi_{21} = \Phi_{12}(\mu_2/\mu_1)(M_1/M_2)$[d]
Binary diffusion coefficient [m^2/s]	Lennard-Jones [28]	$D_{12} = 1.8585 \times 10^{-7} * \mathrm{sqrt}(T^3(1/M_1 + 1/M_2)) * 1/(P\sigma^2_{12}\Omega_{12})$[f]
Enthalpy of water [J/kg]		$h_1 = a + bT + cT^2 + dT^3 + eT^4$; $a = 3.443 \times 10^6$, $b = -4.374 \times 10^3$, $c = 8.618$, $d = -4.515 \times 10^{-2}$, $e = 8.496 \times 10^{-7}$,
Enthalpy of plasma gas [J/kg]		$h_{ar} = a + bT$; $a = -1.551 \times 10^{-1}$, $b = 5.203 \times 10^{-4}$, $h_{ox} = a + bT + cT^2$; $a = -2.849 \times 10^{-1}$, $b = 9.213 \times 10^{-4}$, $c = 7.478 \times 10^{-8}$, $h_2 = h_{ar}Y_{ar} + h_{ox}Y_{ox}$,
Molecular weights [kg/kg mol]		$M_2 = z_{ar}M_{ar} + z_{ox}M_{ox}$; $M_{av} = z_1M_1 + z_2M_2$
Enthalpy of vaporization [J/kg]		$h_{1G} - h_{1L}$

For the liquid, the subindex 1 refers to water and 2 to the anhydrous salt. For the gas, 1 refers to water vapor and 2 for the mixture of argon and oxygen plasma gas.

[a] Experimental values.

[b] The values of Ce^{4+} were approximated from curve fitting values of Gd^{3+} and Sm^{3+}.

[c] The product of these ratios are $(\eta_s/\eta)(\rho_s V_s) \sim 1$.

[d] To obtain μ_2 the same mixing rule was applied but 1 and 2 are argon and oxygen respectively.

[e] The same formulae are used to calculate Φ_{12} and Φ_{21} for the thermal conductivity as for viscosity.

[f] Since argon and oxygen had similar Lennard-Jones potentials, only the values of oxygen are considered which allows the calculation of multicomponent diffusion coefficients. Only, in this case 2 refers to oxygen.

Overall mass conservation

$$-\rho_L \dot{R}|_R = \dot{m} + \int_0^{R(t)} \left(\frac{r}{R}\right)^2 \frac{\partial \rho_L}{\partial t}\, dr \tag{13}$$

At droplet centre

$$\frac{\partial W_i}{\partial r} = \frac{\partial T}{\partial r} = 0 \tag{14}$$

At infinity $r \to \infty$

$$Y_i = 0; \quad T = T_\infty; \quad V = 0; \quad \frac{\partial P}{\partial r} = 0 \tag{15}$$

2.4. Initial conditions

In the liquid phase

$$W_i = W_{i0}, \quad T = T_{L0} \tag{16}$$

In the gas phase

$$Y_i = 0, \quad T = T_{G0}, \quad V = 0, \quad P = P_0 \tag{17}$$

2.5. Thermophysical properties

A more accurate formulation of the problem can be derived taking into account temperature and concentration dependence of the liquid and gas properties (Table 1).

2.6. Solution procedure

Comsol Multiphysics® was used to solve the model. The model consisted of ~12,300 elements distributed in a non-uniform mesh, where a higher number of elements were located at the droplet interface. Mesh independent solutions were obtained. Quadratic Lagrange elements were used for all variables with the exception of pressure in which linear elements were employed. Lagrange multipliers were used to improve solution convergence of the boundary conditions. A Heaviside step function [20] was applied to provide smooth temperature and concentration profiles as initial conditions in the vicinity of the droplet interphase.

3. Model validation

The model was validated by comparing the ratio of the surface concentration (C_s) to the mean concentration (C_m) minus one ($C_s/C_m - 1$) of a non-volatile solute in an

Table 2
Experimental ranges of studied variables

T_∞ [K]	W_{s0}	P [atm]	z_{Ar}/z_{O_2}	D [μm]
500	0.3	**0.3**	0.2/0.8	20
600	0.4	0.4	**0.3/0.7**	**30**
700	**0.5**	0.5	0.4/0.6	40

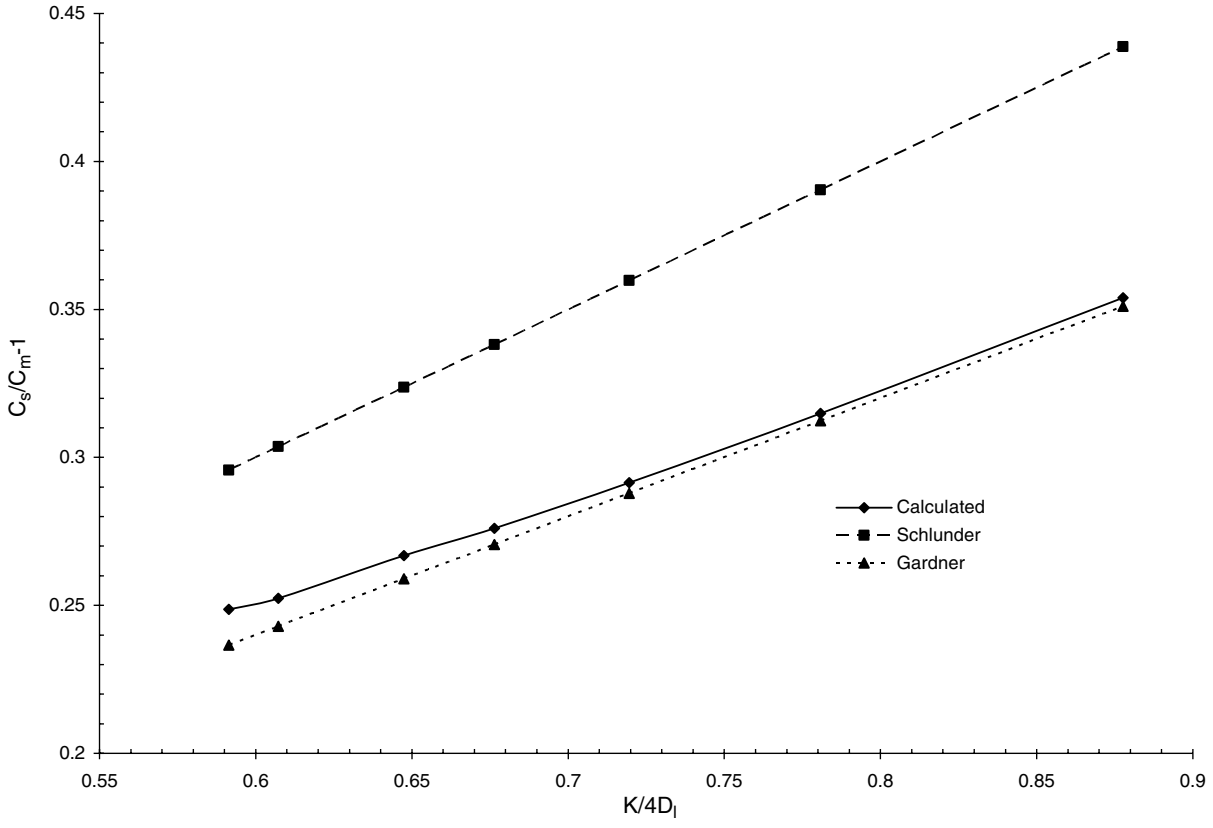

Fig. 2. Model validation.

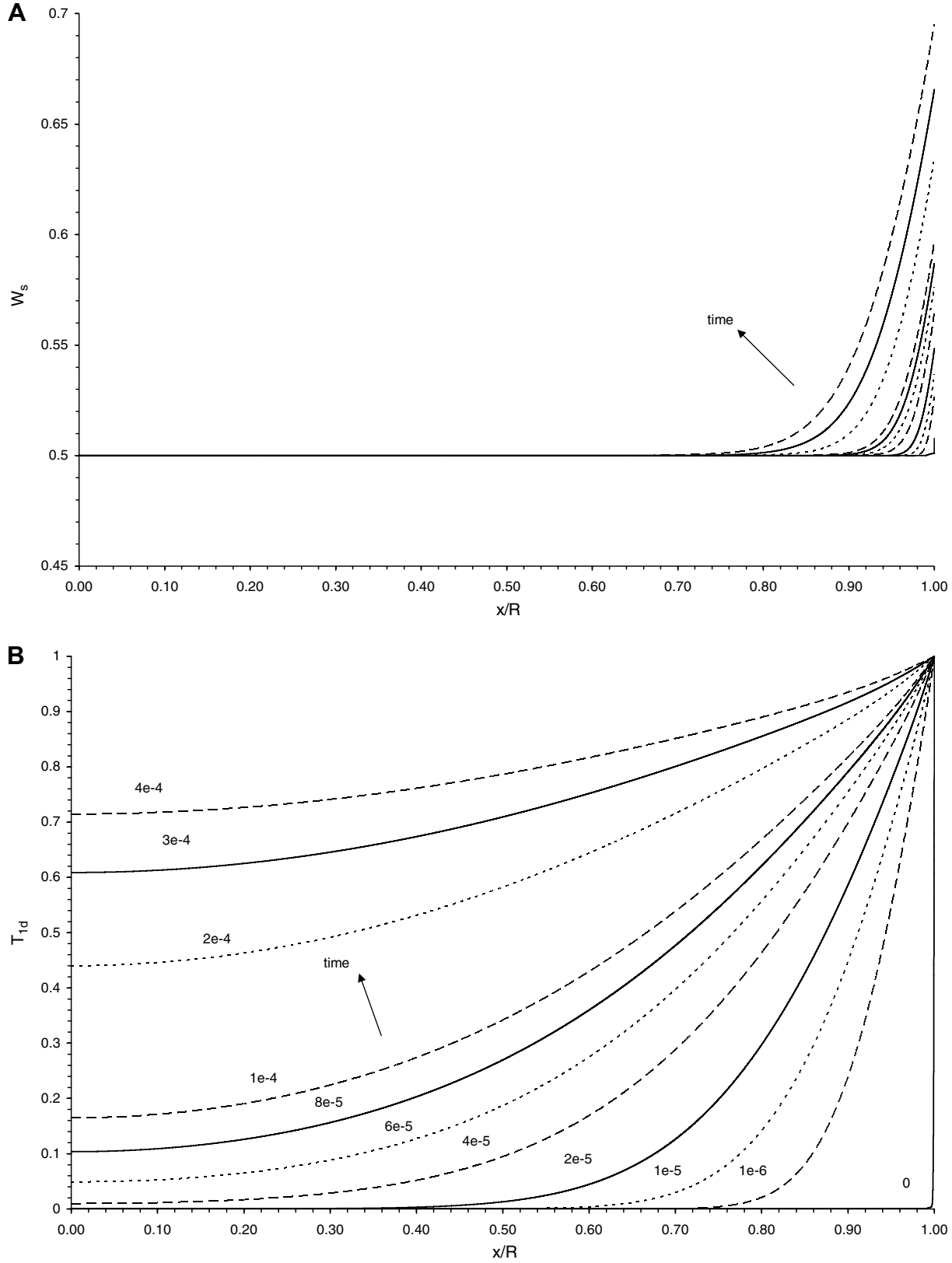

Fig. 3. Mass fraction and temperature profiles in the droplet as a function of radial position for different times ($T_\infty = 600$ K, $W_{s0} = 0.5$, $P = 0.3$ atm, $z_{Ar} = 0.3/zO_2 = 0.7$, $D = 30$ μm, $t = 0$ to 4×10^{-4} s. Same times in figure A and B).

evaporating drop. These values were estimated by Schlünder [14] and further re-computed by Gardner [15]. Schlünder confirmed experimentally that the ratio approached a constant asymptotic value, which allowed the simplifica-

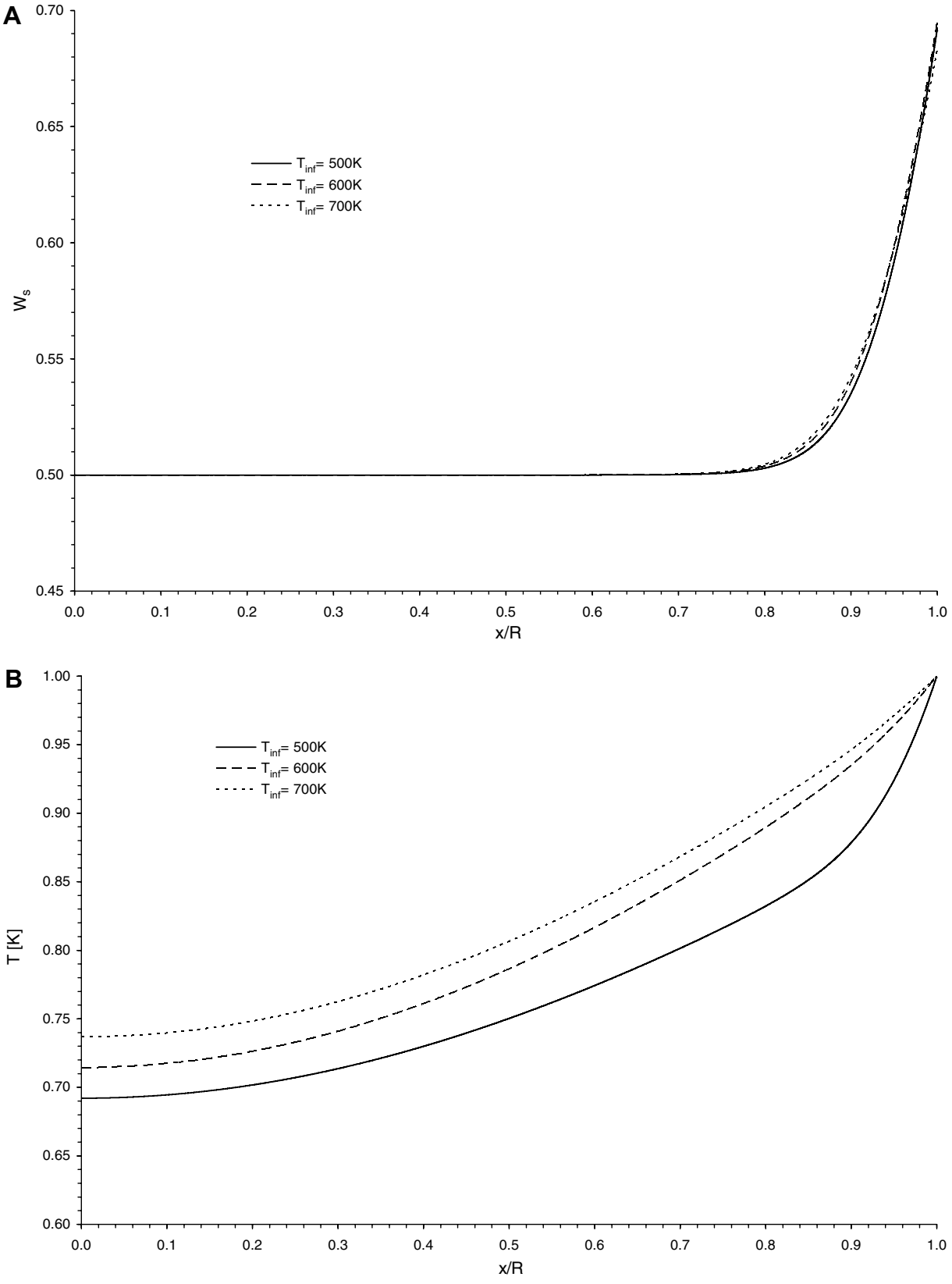

Fig. 4. Mass fraction and dimensionless temperature radial profiles in the droplet as a function of plasma temperature at $t = 4 \times 10^{-4}$ s ($W_{s0} = 0.5$, $P = 0.3$ atm, $z_{Ar} = 0.3/zO_2 = 0.7$, $D = 30$ μm).

tion of equations describing the transient mass transfer inside the droplet. Gardner further formalized that simplification by stating that the product of $R_{(t)}\mathrm{d}R_{(t)}/\mathrm{d}t$ was constant for the most part during evaporation. In these studies

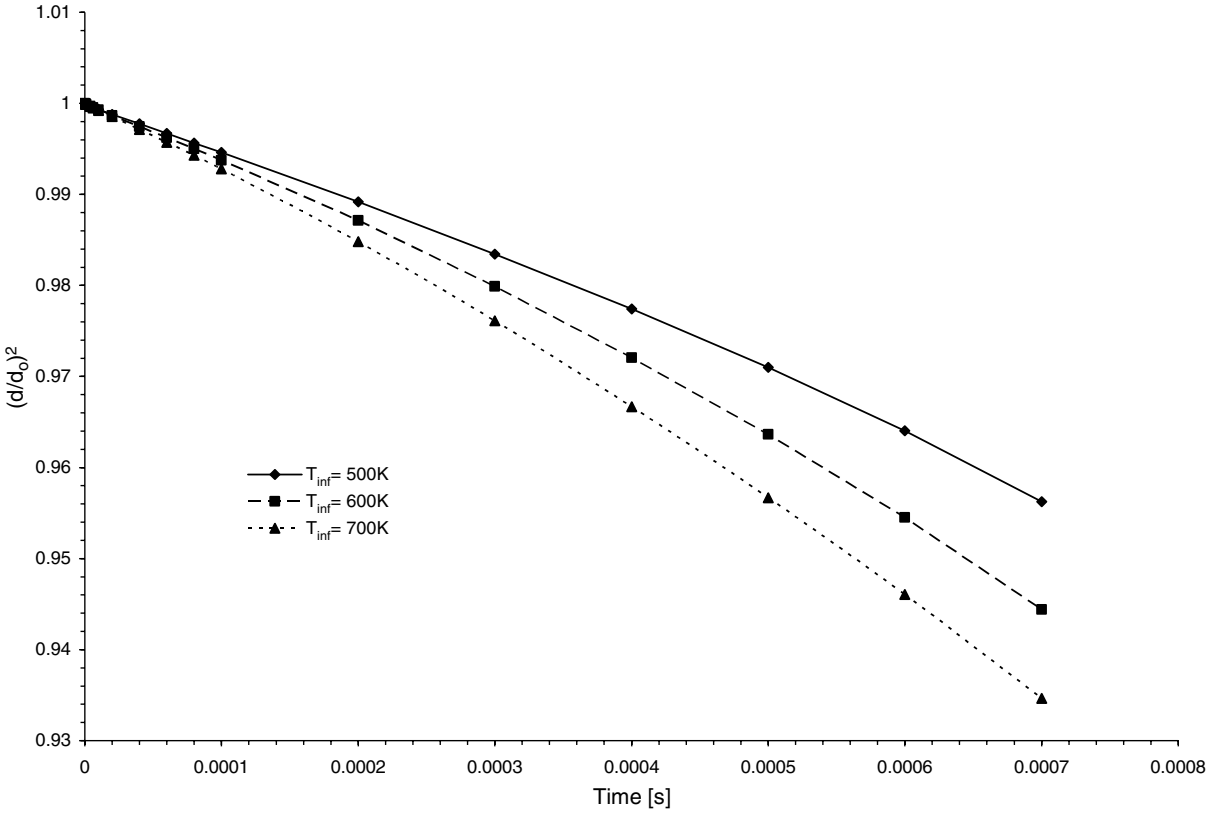

Fig. 5. Evolution of droplet diameter as a function of time for different plasma temperatures ($W_{s0} = 0.5$, $P = 0.3$ atm, $z_{Ar} = 0.3/zO_2 = 0.7$, $D = 30$ μm).

it was assumed that the diffusion coefficient of the salt in the solution droplet was constant. The model presented in this study was in agreement with Gardner's findings with less than 1.5% error and showed that Schlünder's results were off by roughly 20%, but that both had similar trends (Fig. 2). It is worth noting that this agreement was confirmed for low values of $K/4D_L$ and a constant value of D_L was used to match their calculations. Further, the work of Xiong and Kodas [16] also based their findings on Gardner's approach to investigate the evolution of the droplet size in spray pyrolysis of sodium chloride aqueous solution droplets; thus, giving credit to this method as a form of model validation.

4. Results and discussion

The present simulation considered the effects of plasma temperature, initial salt concentration, system pressure and initial particle size on the temperature and mass profiles in the evaporating droplet. The simulations were stopped when the mass fraction of salt approached the supersaturation limit, i.e. $W_s = 0.7$ (this limit was experimentally determined). In most cases, the supersaturation limit was reached in approximately 4×10^{-4} s (almost half of a millisecond). Table 2 summarizes all the conditions analyzed in this paper; the base case is given in bold. For instance, to analyze the pressure of the system, all the other parameters were $T_\infty = 600$ K, W_{s0}=0.5, $z_{Ar} = 0.2$, $D = 30$ μm at different pressures, $P = 0.3$, 0.4 and 0.5 atm. The conditions for temperature at infinity are typical of rf plasma systems where the liquid injection into the hot core of the plasma causes a local quenching and thus temperatures below 800 K are expected [21].

The salt mass fraction and dimensionless temperature $T_{1d} = (T - T_{L0}/(T_s - T_{L0}))$ profiles in the droplet are shown in Fig. 3a and b. The radial position plotted is referred to the moving frame which follows the droplet decrease in size over time. The results indicate that the temperature profile is clearly developed and has reached the centre of the droplet prior to the moment of expected solute precipitation at R (droplet surface). On the contrary, the developing of the salt mass fraction profile is much slower. There is a large mass fraction difference (i.e. from 0.5 to 0.7) in the vicinity of the droplet surface, whereas the remaining of the droplet still remains at its initial value. The differences in profiles are because heat transfer by conduction is much faster than diffusion mass transfer. As a result, a growing crust is expected to form at the droplet surface where the supersaturation point has been reached.

4.1. Effect of plasma temperature

The surrounding plasma temperature (T_∞) was increased from 500 K to 700 K and the results are presented in Fig. 4a and b at 4×10^{-4} s (onset of solute nucleation at the surface). It can be seen that the mass fraction

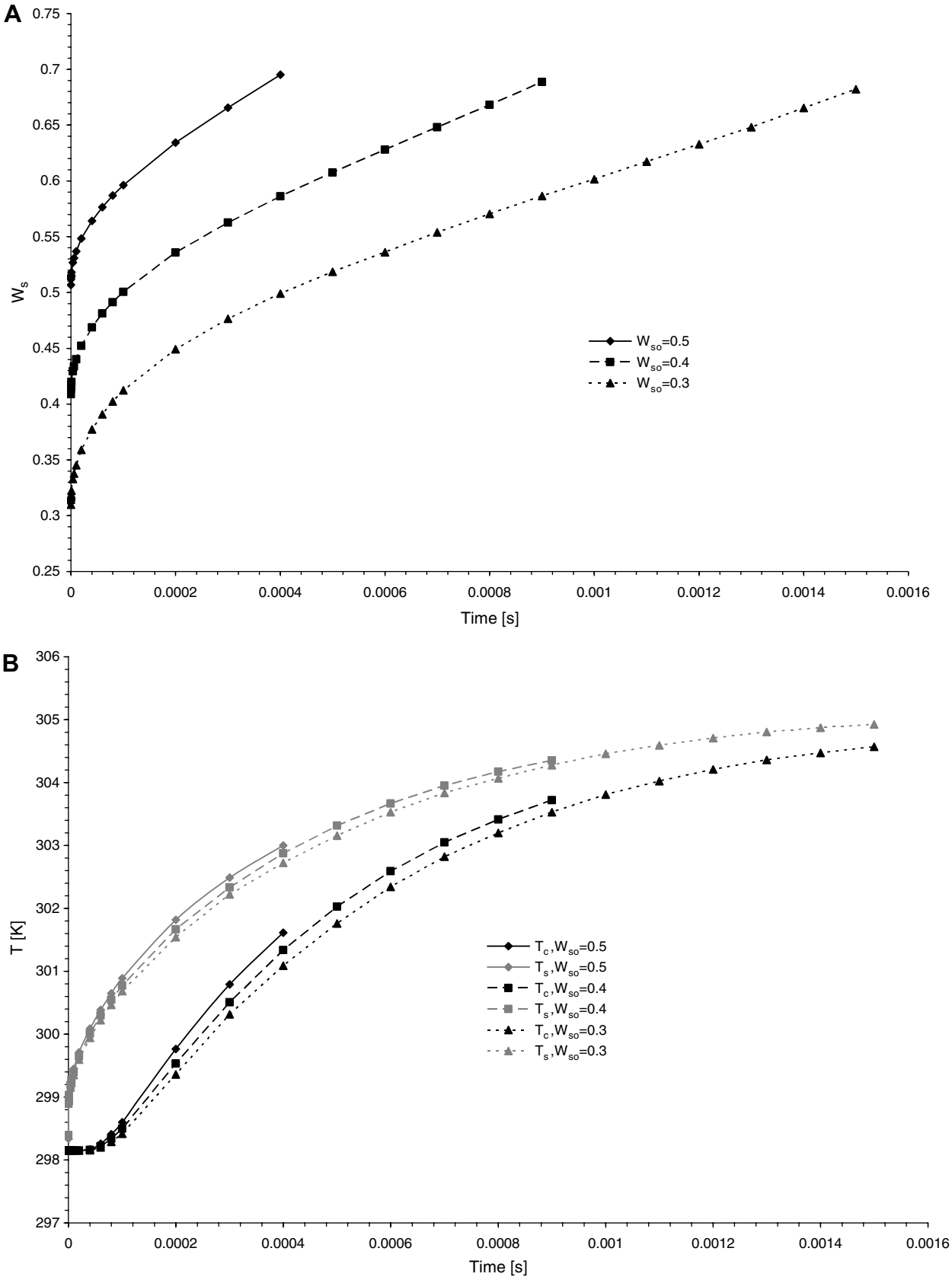

Fig. 6. Mass fraction profile at the droplet surface as a function of time. Temperature profiles at the droplet centre and surface as a function of time ($T_\infty = 600$ K, $P = 0.3$ atm, $z_{Ar} = 0.3/zO_2 = 0.7$, $D = 30$ μm).

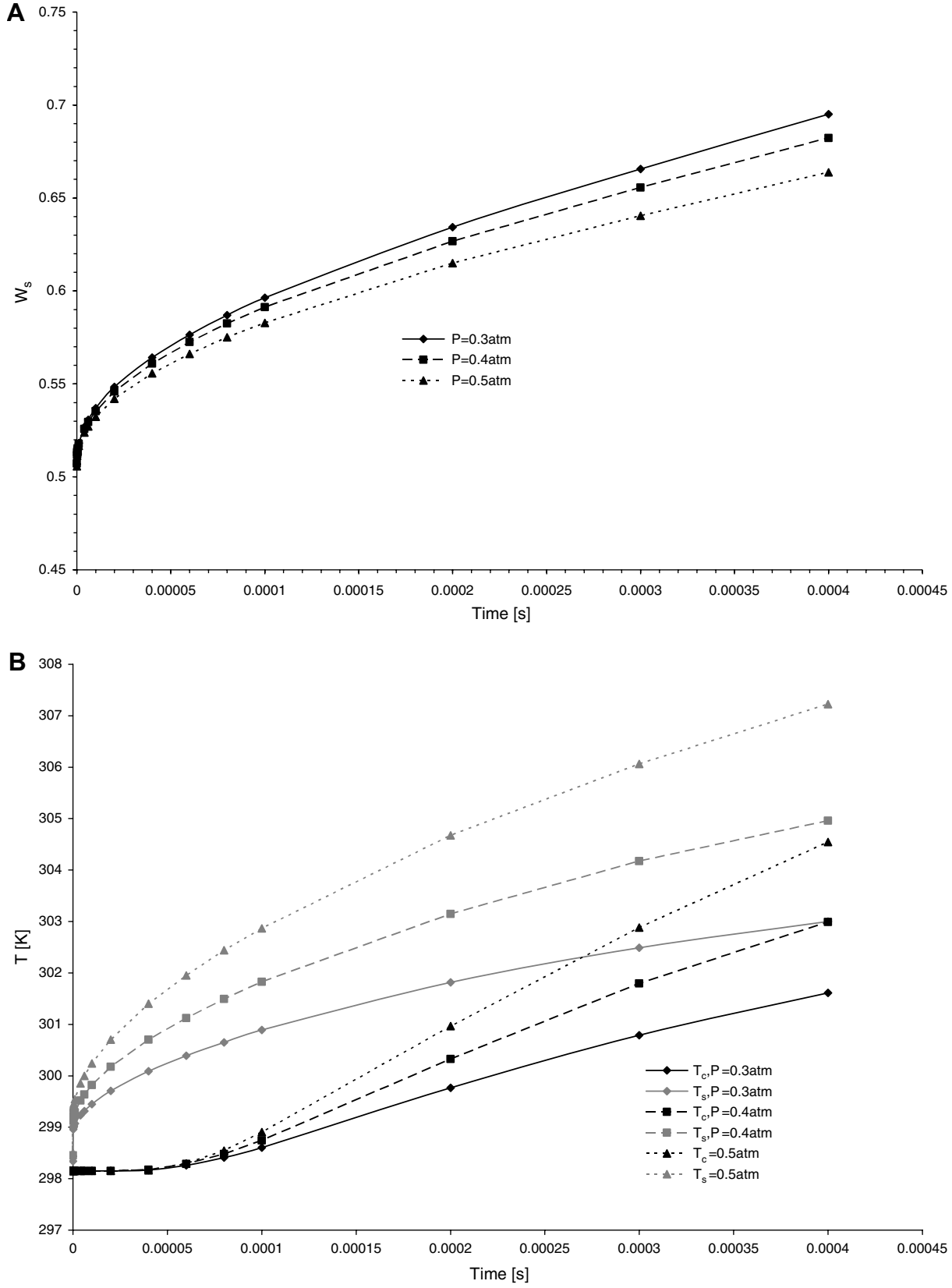

Fig. 7. Mass fraction profile at the droplet surface as a function of time. Temperature profiles at the droplet centre and surface as a function of time ($T_\infty = 600$ K, $W_{s0} = 0.5$, $z_{Ar} = 0.3/zO_2 = 0.7$, $D = 30$ μm).

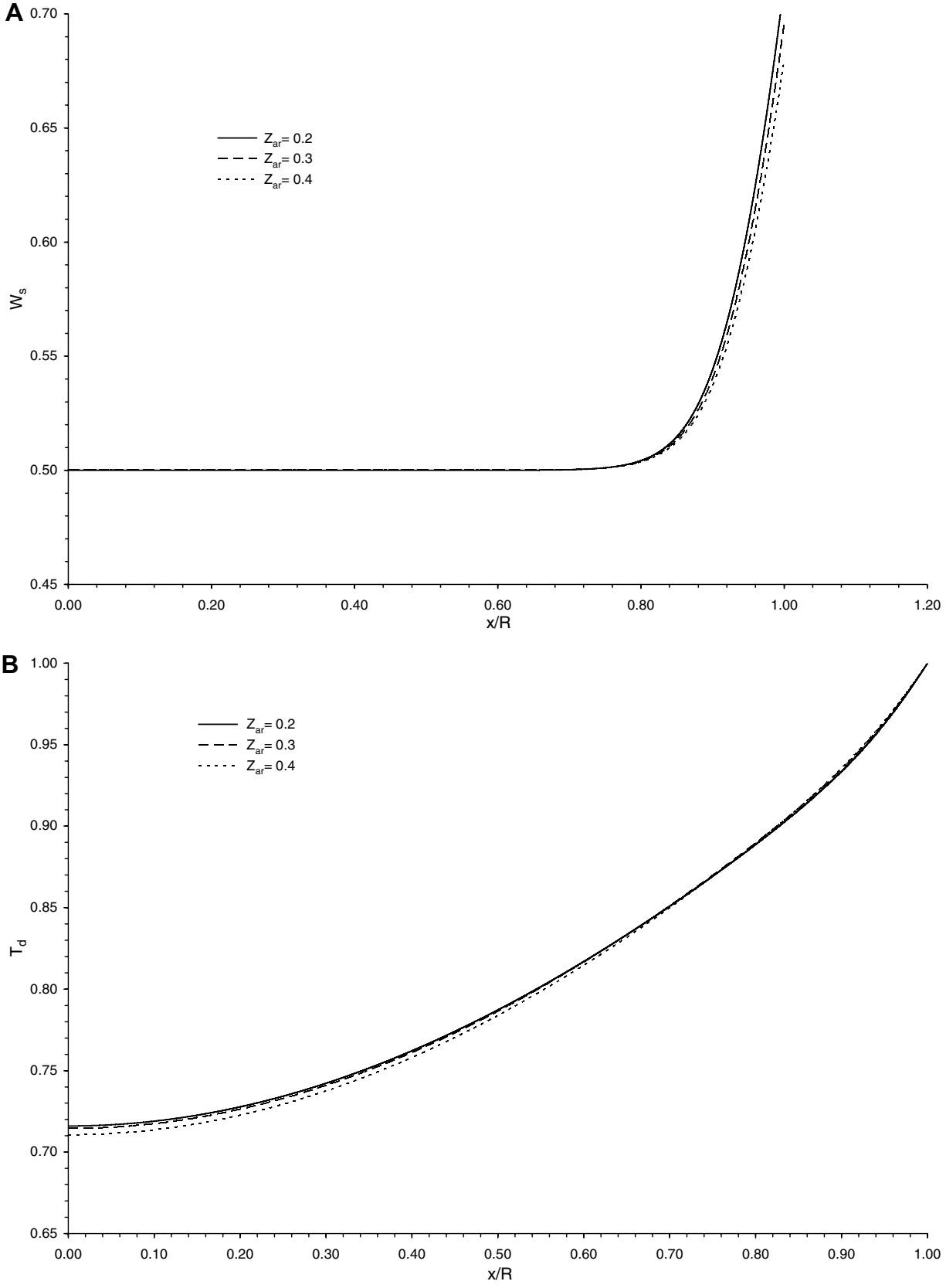

Fig. 8. Mass fraction and dimensionless temperature radial profiles in the droplet as a function of plasma gas composition at $t = 4 \times 10^{-4}$ s ($T_\infty = 600$ K, $W_{s0} = 0.5$, $P = 0.3$ atm, $D = 30$ μm).

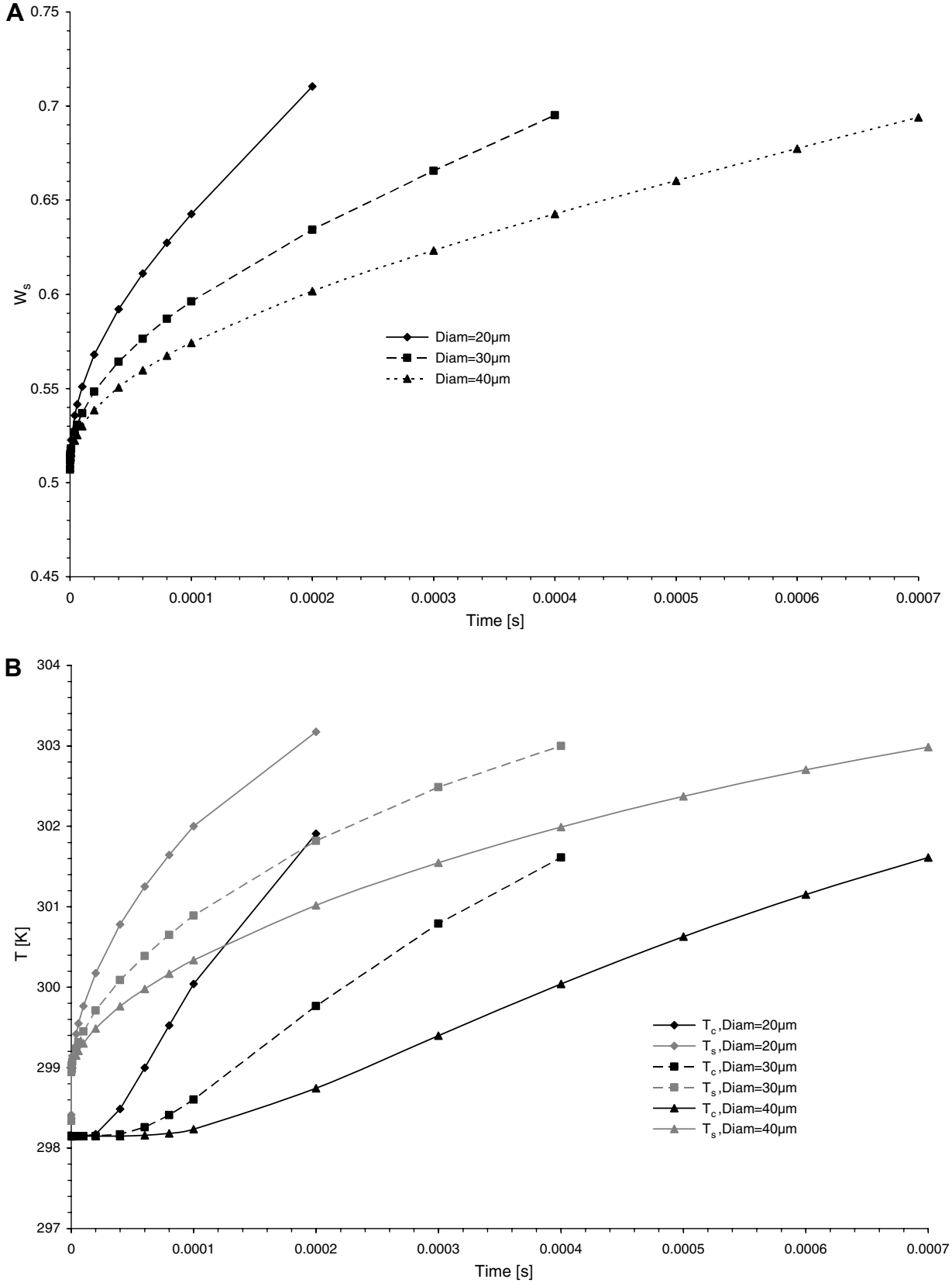

Fig. 9. Mass fraction profile at the droplet surface as a function of time. Temperature profiles at the droplet centre and surface as a function of time ($T_\infty = 600$ K, $W_{s0} = 0.5$, $P = 0.3$ atm, $z_{Ar} = 0.3/zO_2 = 0.7$).

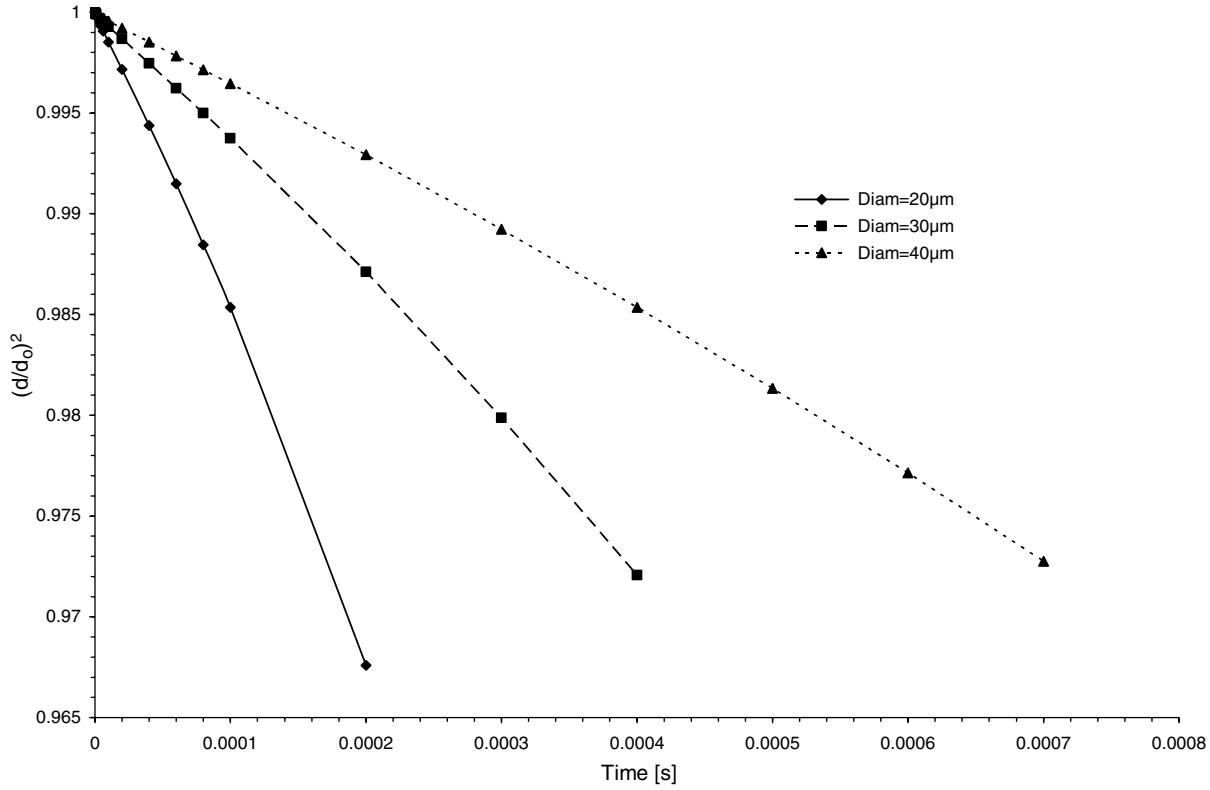

Fig. 10. Evolution of droplet diameter as a function of time for different initial droplet sizes ($T_\infty = 600$ K, $W_{s0} = 0.5$, $P = 0.3$ atm, $z_{Ar} = 0.3/zO_2 = 0.7$, $D = 30$ μm).

of salt is only slightly affected by the increase of plasma gas temperature. It appears that more salt diffuses towards the centre of the droplet as the temperature increases, since mass diffusivity increases with increasing temperature. However, this effect is minor. On the other hand, the temperature profile inside the droplet is affected strongly. Higher plasma temperatures result in more energy transfer to the droplet. Therefore, higher temperatures are expected in the evaporating droplet at the beginning of solute precipitation.

The change of droplet diameter at different plasma temperatures is illustrated in Fig. 5, where the ratio of the droplet diameter (d) to the original diameter (d_o) is shown as a function of time. As expected, as the temperature of the plasma gas is augmented, more water is vaporized and thus the droplet decreases in size at a faster rate. The graph shows that the droplet has not significantly decreased in size (almost 96% of the original size remains) when its surface has already reached the point of supersaturation.

4.2. Effect of initial salt content

The initial salt content was varied from $W_s = 0.3$ to $W_s = 0.5$. The salt mass fraction at the surface (Fig. 6a) and the temperature at the centre and surface of the droplet were plotted (Fig. 6b) as a function of time. The mass profile indicates that there are two regions. First, a rapid change of mass content happens before 2×10^{-4} s, and second, the mass fraction varies almost linearly until the limit of supersaturation is achieved. There is no apparent change in the way the vaporization occurs or the crust is formed as a function of initial solute content. The differences among the different initial solute concentrations are more related to the time taken to reach the onset of crust formation. The less solute is present (thus more solvent), the longer it takes for the appearance of a crust. Similarly, the temporal temperature profiles in the centre and at the droplet surface do not show a distinct variation as more solvent is present in the droplet. Initially, the temperatures at the centre and surface are the same. Then there is a temperature gradient that increases with time, and towards the end this gradient slowly decreases as heat is conducted throughout the droplet.

In summary, the addition of solvent to the droplet has the effect of retarding the formation of a crust as a result of a longer evaporation time. The results showed that mass diffusion and heat conduction are weak functions of concentration for the range studied, even though density, thermal conductivity, heat capacity and mass diffusivity were all functions of solute content.

4.3. Effect of system pressure

The system pressure was varied from 0.3 atm to 0.5 atm since most of the rf thermal plasmas used in this type of

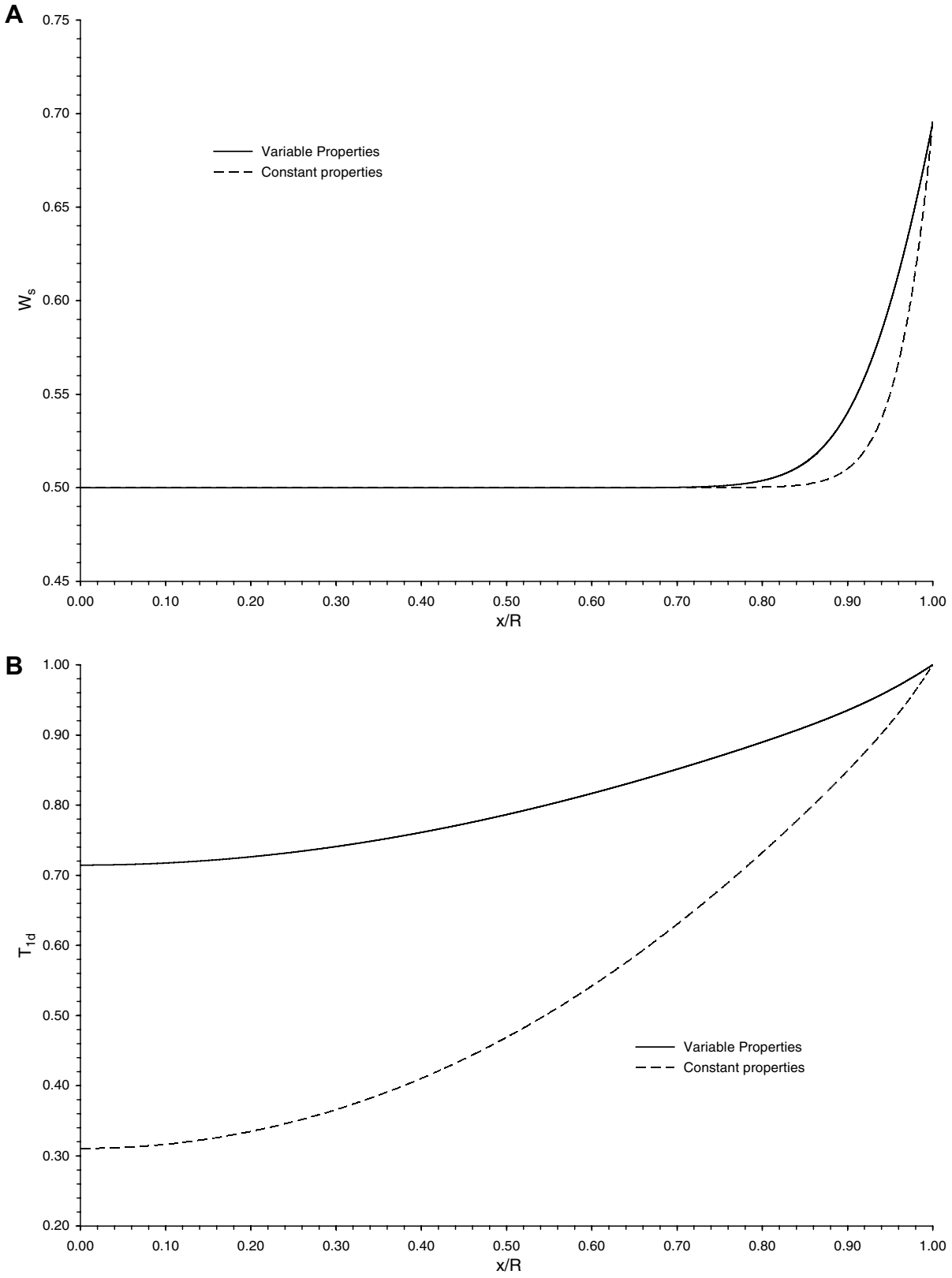

Fig. 11. Mass fraction and dimensionless temperature radial profiles in the droplet as a function of plasma temperature at $t = 4 \times 10^{-4}$ s ($T_\infty = 600$ K, $W_{s0} = 0.5$, $P = 0.3$ atm, $z_{Ar} = 0.3/zO_2 = 0.7$, $D = 30$ μm).

application operate under reduced pressure. The surface salt content and the surface temperature and the centre droplet temperature are plotted as a function of time in Fig. 7a and b, respectively. Reducing the pressure, reduces

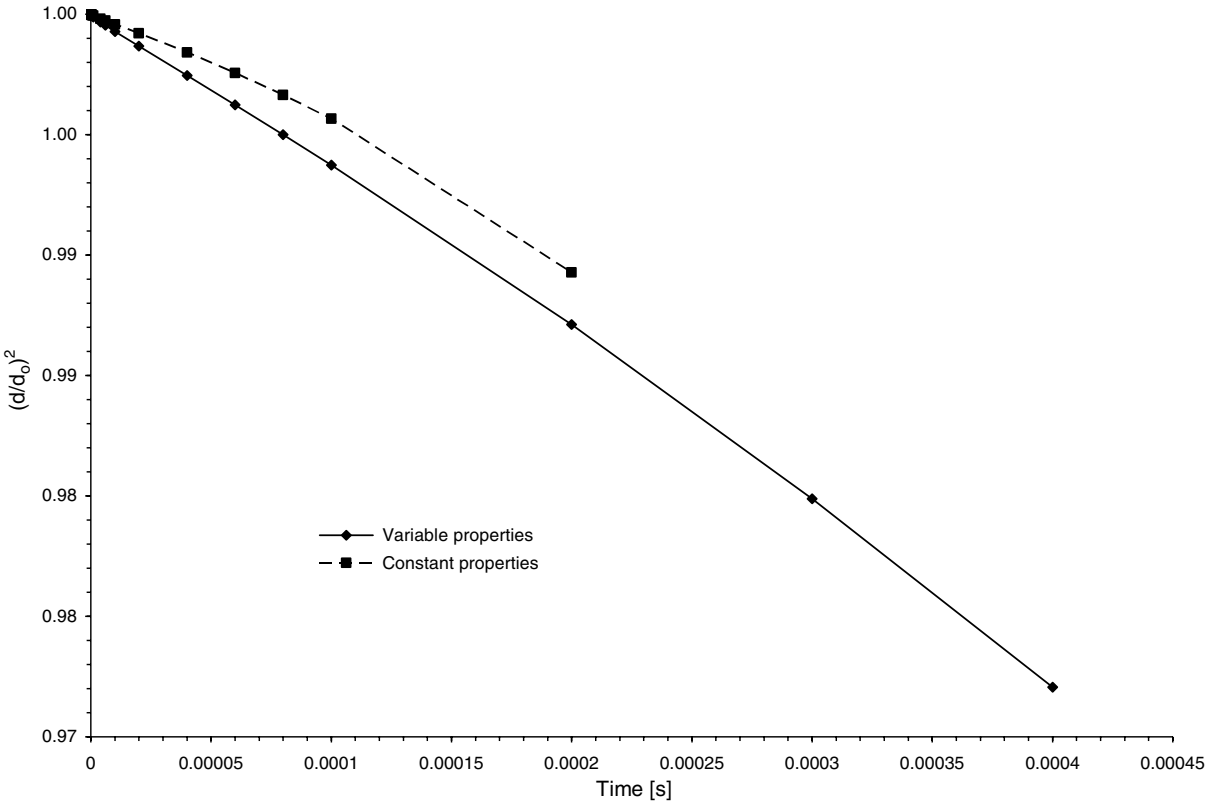

Fig. 12. Evolution of droplet diameter as a function of time for constant and variable thermophysical properties ($T_\infty = 600$ K, $W_{s0} = 0.5$, $P = 0.3$ atm, $z_{Ar} = 0.3/zO_2 = 0.7$, $D = 30$ μm).

the boiling temperature of the droplet which favors solvent vaporization. Also, because the water is vaporizing into Ar and O_2, the boiling point is further lowered. As a result, the droplet surface temperature is only a few degrees above room temperature when the droplet salt content at the droplet–gas interface reaches supersaturation values. Further, lower pressures cause a faster achievement of the nucleation point at a lower temperature. As expected, the boiling temperature of the droplet surface is higher with increasing pressure and the difference between centre and surface temperatures is larger during the early stages of evaporation.

As a conclusion, the lower the pressure, the faster the onset of crust formation for a given set of operating parameters.

4.4. Effect of plasma composition

The plasma gas composition was changed from 0.2/0.8 argon–oxygen (in mol fraction) to a 0.4/0.6 argon–oxygen mixture. These are typical operating ranges in rf thermal plasmas. The salt content temperature profiles at the onset of crust formation were plotted as a function of radial position (Fig. 8a and b). An oxygen-rich plasma has a higher enthalpy at the same temperature. The results suggest that this change of enthalpy has a small effect on the salt diffusion and water evaporation, judging from the similarity of the profiles in all cases. It is also shown that the limit of supersaturation is achieved slightly faster when an oxygen-rich plasma is employed.

The effect of plasma composition could be more important as the temperature of the surrounding gas increases (>3000 K), especially because, the thermal conductivity of oxygen increases greatly with temperature. However, this range was out of the operating window of the present study.

4.5. Effect of initial droplet size

Three different initial droplet sizes were tested, i.e. 20 μm, 30 μm, and 40 μm. Salt content and temperature values were plotted as a function of time (Fig. 9a and b). The results clearly indicate that droplet size has a major effect on the crust-formation and evaporation processes. Smaller droplets reached the point of crust formation faster than larger droplets and the difference between the surface and centre temperature does not seem to depend on droplet size. Despite the small droplet diameter, temperature and salt mass fraction are different from the centre to the surface.

The change of droplet diameter with time is illustrated in Fig. 10. The larger droplets show a less pronounced slope and thus take longer to evaporate. Despite the change in size, the phenomena affecting evaporation remain largely unchanged, i.e. faster heat conduction due to smaller

droplet sizes and slow development of mass fraction profiles as a result of mass diffusion.

4.6. Comparison between constant and variable properties

The model was solved with constant and variable properties to assess the effect on the predicted mass and temperature profiles. The results are presented in Figs. 11a and b and 12. The use of constant properties under predicts the development of the mass and temperature profiles inside the droplet and it also under estimates the droplet size change. Therefore, the use of variable properties provides a more realistic and accurate calculation of the onset of crust formation and droplet evaporation.

5. Conclusions

The present work shows that crust formation in an evaporating solution droplet containing non-volatile compounds is present in all cases. The change of parameters demonstrated that all conditions that favor vaporization will tend to promote crust formation in less time, i.e. higher temperatures, more enthalpic plasma gas, less solvent, lower pressure. Further, the initial droplet size has a marked effect on the time at which crust formation is achieved, and thus rendering droplet size an important parameter to control in rf thermal plasmas.

A crust is formed in all cases as a result of salt precipitation. The slower rate of mass transfer inside the droplet in comparison with the faster heat transfer rate by conduction is responsible for crust formation. Also, the use of temperature and composition variable properties in both the gas and liquid phases results in a more realistic model with increasing predicting scope.

The fact that the supersaturation point is always achieved within the operating range studied at the droplet surface provides encouraging evidence to support droplet explosion. As a result of pressure buildup in the inner core of an evaporating droplet in rf thermal plasma systems.

Acknowledgements

The financial support by the Natural Sciences and Engineering Research Council of Canada and the Ministry of Education of the Province of Quebec through its FQRNT program is gratefully acknowledged.

References

[1] E. Bouyer, F. Gitzhofer, M.I. Boulos, Suspension plasma spraying for hydroxyapatite powder preparation by rf plasma, IEEE Trans. Plasma Sci. 25 (5) (1997) 1066–1072.
[2] M. Müller et al., Thermal induction plasma processes for the synthesis of SOFC materials, Materialwiss. Werkstofftech. 33 (6) (2002) 322–330.
[3] E. Bouyer et al., Thermal plasma chemical vapor deposition of Si-based ceramic coatings from liquid precursors, Plasma Chem. Plasma Process. 21 (4) (2001) 523–546.
[4] Delbos et al., DC plasma spray elaboration of fine structured coatings by ceramic liquid suspension injection, in: Proceedings 16th International Symposium on Plasma Chemistry (ISPC 16), Italy, 2003.
[5] Y.C. Lau, P.C. Kong, E. Pfender, Synthesis of zirconia powders in an RF plasma by injection of inorganic liquid precursors, Ceram. Trans. 1 (1988) 298–303.
[6] F. Gitzhofer et al., Integrated fabrication processes for solid-oxide fuel cells using thermal plasma spray technology, MRS Bull. 25 (7) (2000) 38–42.
[7] Fauchais et al., Plasma spraying from thick to thin coatings and micro to nano-structured coatings, in: Proceedings 16th International Symposium on Plasma Chemistry (ISPC 16), Italy, 2003.
[8] I. Castillo, R. Munz, Inductively coupled plasma synthesis of CeO_2-based powders from liquid solutions for SOFC electrolytes, Plasma Chem. Plasma Process. 25 (2) (2005) 87–107.
[9] L. Jia, F. Gitzhofer, Collection of nano-powders generated by radio frequency (RF) plasma spray synthesis (PSS) processing, using a sampling probe, in: Proceedings 17th International Symposium on Plasma Chemistry (ISPC 17), Canada, 2005.
[10] H. Yu, W.H. Liao, Evaporation of solution droplets in spray pyrolysis, Int. J. Heat Mass Transfer 41 (8–9) (1997) 993–1001.
[11] D.H. Charlesworth, W.R. Marshall, Evaporation from drops containing dissolved solids, AIChE J. 6 (1) (1960) 9–23.
[12] T. Elperin, B. Krasovitov, Evaporation of liquid droplets containing small solid particles, Int. J. Heat Mass Transfer 38 (12) (1995) 2259–2267.
[13] A. Ozturk, B.M. Cetegen, Modeling of plasma assisted formation of precipitates in zirconium containing liquid precursor droplets, Mater. Sci. Eng. A 384 (2004) 331–351.
[14] E.U. Schlünder, Temperatur- und Masseänderung verdunstender Tropfen aus reinen Flüssigkeiten und wässrigen Salzlösungen, Int. J. Heat Mass Transfer 7 (1964) 49–73.
[15] G.C. Gardner, Asymptotic concentration distribution of an involatile solute in an evaporating drop, Int. J. Heat Mass Transfer 8 (1965) 667–668.
[16] Y. Xiong, T.T. Kodas, Droplet evaporation and solute precipitation during spray pyrolysis, J. Aerosol Sci. 24 (7) (1993) 893–908.
[17] G.V. Jayanthi, S.C. Zhang, G.L. Messing, Modeling of solid particle formation during solution aerosol thermolysis, Aerosol Sci. Technol. 19 (4) (1993) 478–490.
[18] J. Donea et al., Arbitrary Lagrangian–Eulerian methodsEncylcopedia of Computational Mechanics, vol. 1, John Wiley & Sons, 2004 (Chapter 14).
[19] Comsol, Comsol Multiphysics: Modeling Guide, Version 3.2, 2005.
[20] Heaviside functions. Available from: <http://mathworld.wolfram.com/HeavisideStepFunction.html>.
[21] V. Colombo, E. Ghedini, A. Mentrelli, 3-D Turbulent modeling of an ICPT with detailed gas injection section, in: Proceeding of the ISPC 16, Canada, 2005.
[22] Y.S. Touloukian, T. Makita, Thermophysical Properties of Matter: Specific Heat of Non-metallic Liquids and Gases, vol. 6, Plenum, 1970.
[23] J.A. Dean, Lange's Handbook of Chemistry, Fifteenth ed., McGraw-Hill, 1999.
[24] R.C. Reid et al., The Properties of Gases and Liquids, fourth ed., McGraw-Hill, 1987.
[25] J. Rard et al., Isopiestic determination of the activity coefficients of some aqueous rare earth electrolyte solutions at 25 °C, J. Chem. Eng. Data 22 (3) (1977).
[26] A. Vasic, A. Cheng, D.C. Groeneveld, A comparison of predictions of high-temperature steam properties, Nucl. Eng. Des. 132 (1992) 367–379.
[27] M.I. Boulos, P. Fauchais, E. Pfender, Thermal plasmas, Fundamentals and Applications, vol. 1, Plenum, 1994.
[28] R.B. Bird, W.E. Stewart, E.N. Lightfoot, Transport Phenomena, second ed., John Wiley & Sons, 2002.